NANO LETTERS

pubs.acs.org/NanoLett Letter

Atomic-Scale Hidden Point-Defect Complexes Induce Ultrahigh-Irradiation Hardening in Tungsten

Ruo-Yao Zheng, Wu-Rong Jian, Irene J. Beyerlein, and Wei-Zhong Han*

Cite This: Nano Lett. 2021, 21, 5798−5804 Read Online

ACCESS | Metrics & More | Article Recommendations | Supporting Information

ABSTRACT: Tungsten displays high strength in extreme temperature and radiation environments and is considered a promising plasma facing material for fusion nuclear reactors. Unlike other metals, it experiences substantial irradiation hardening, which limits service life and presents safety concerns. The origin of ultrahigh-irradiation hardening in tungsten cannot be well-explained by conventional strengthening theories. Here, we demonstrate that irradiation leads to near 3-fold increases in strength, while the usual defects that are generated only contribute less than one-third of the hardening. An analysis of the distribution of tagged atom−helium ions reveals that more than 87% of vacancies and helium atoms are unaccounted for. A large fraction of helium−vacancy complexes are frozen in the lattice due to high vacancy migration energies. Through a combination of in situ nanomechanical tests and atomistic calculations, we provide evidence that irradiation hardening mainly originates from high densities of atomic-scale hidden point-defect complexes.

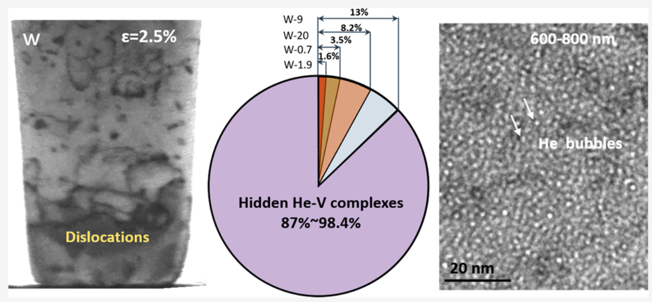

KEYWORDS: *Tungsten, Irradiation, Hardening, Helium, Dislocation*

Fusion promises unlimited energy for mankind. Unfortunately, however, 14.1 MeV fusion neutrons activate many nuclides (such as Ni) and also leave helium (He) inside the material.[1] Low-activation elements, such as tungsten (W), vanadium, and iron, are becoming the most promising elements for structural metals.[2,3] However, this class of metals has a body-centered cubic (BCC) crystal structure, which tends to exhibit substantial increases, by more than 100%, in yield strength, when exposed to irradiation.[4−13] This phenomenon, known as irradiation hardening, is several times more severe in BCC metals than that in face-centered cubic (FCC) and hexagonal close-packed metals (HCP).[14−18] More importantly, such ultrahigh-irradiation hardening (UIH) is ubiquitous in BCC metals[4−13] and cannot be accurately estimated on the basis on observed nanoscale irradiation defects (i.e., bubbles, voids, or dislocation loops). Most theories for hardening are based on knowledge of the density and size of these irradiation-induced imperfections, yet, still, by considering only those visible defects, some of them lead to predictions that are much lower than experimentally measured hardening.[4−13] UIH is harmful and unpredictable and deteriorates the performance of refractory metals when in service in extreme environments.

Tungsten, a typical refractory metal, is regarded as an ideal candidate for plasma facing materials in fusion nuclear reactors due to its high melting temperature, low sputtering yields, and small evaporative coefficients.[19,20] During fusion reactor operation, W is exposed to high-flux neutron irradiation, bombardments from light-ion plasmas, and high-heat fluxes.[19,20] The light ions are implanted into W and tend to combine with irradiation-induced vacancies to form gas bubbles.[21] The result is a substantial increase in yield strength, by several times, and also in strain hardening.[4−13] Like other BCC metals,[4−13] W exhibits UIH, where all traditional model estimates prove to be much less than the experimentally observed hardening.[5,6] UIH in W further reduces the toughness and ductility of this already brittle material. UIH in BCC metals is thought to be related to unusually large quantities of point defects that are produced during irradiation but invisible to current microscopy techniques.[22−24] Such defects would be atomic-scale defects, distinct from the usual relatively larger defect clusters, such as nanoscale loops, voids, or bubbles. By the very nature of their fine size, garnering direct supporting experimental evidence of their composition, density, and size has been challenging.

Here, we investigate the irradiation hardening in He-implanted single crystal W. He ions were used as tagged atoms to track the distribution of irradiation-induced point defects. We combine nanomechanical testing, transmission electron microscopy, and molecular dynamics (MD) simu-

Received: April 25, 2021
Revised: June 29, 2021
Published: July 6, 2021

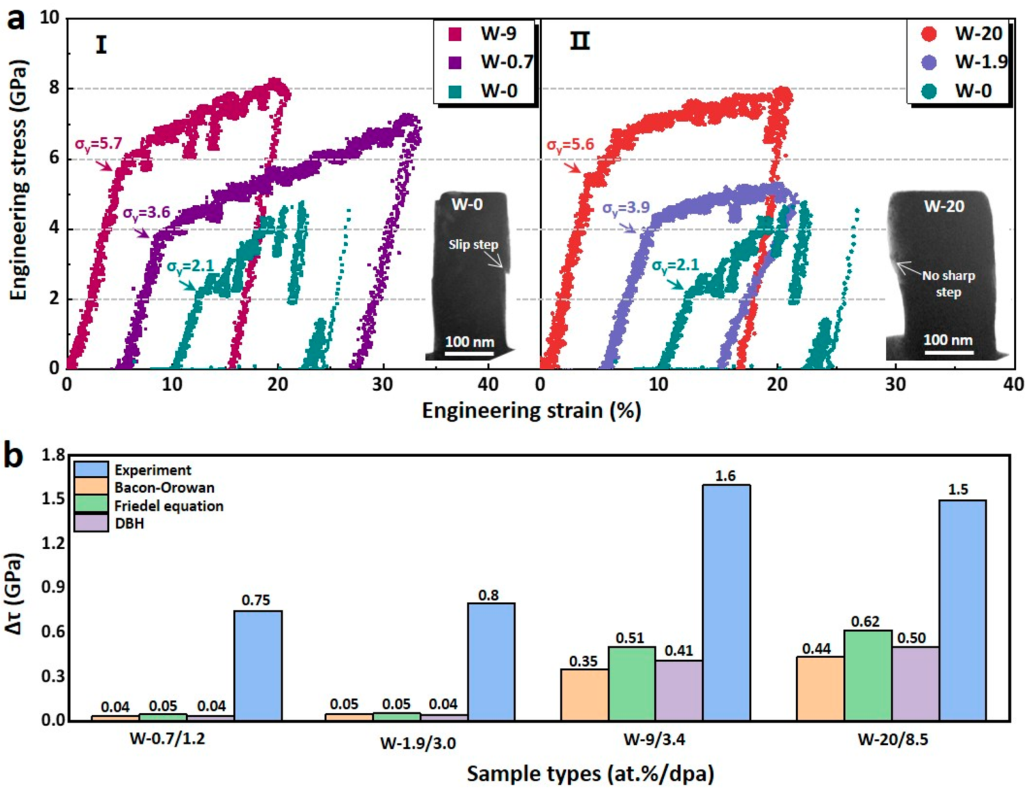

Figure 1. Anomalous strengthening in irradiated W. (a) Engineering compressive stress−strain curves of W pillars with different levels of radiation defects. (b) Comparison of strengthening in irradiated W measured in experiments and predicted by models.

lations to reveal the mechanisms of irradiation hardening. Detailed information for the experimental and simulation methods can be found in the Supporting Information (SI).

Figure 1a shows the typical compressive stress−strain curves for single crystals of W with different levels of He concentration and radiation damage, ranging from 0 to 20 at. %. For reference, we observe the stress−strain response of the pure W pillar, W-0 (no He), which yields at a stress level of around 2.1 GPa and exhibits classic signs of inhomogeneous deformation. Its stress−strain response after yielding features frequent strain bursts, as marked in the figure. These bursts are correlated with the formation of sharp slip steps on the crystal surface. The stress−strain responses of irradiated W have increasingly higher yield strengths as the He concentration increases to 0.7 at. % (W-0.7), 1.9 at. % (W-1.9), and up to 9 at. % (W-9). The yield strengths of W-9 and W-20 (20 at. %) are similar, reaching 2.7 times that of pure W-0. The irradiated material response shows stable deformation without unstable strain bursts. The insets in Figure 1a(II) further indicate homogeneous deformation. The irradiated pillars also experience significant strain hardening.

To understand how irradiation affects the underlying dislocation dynamics during deformation, we performed in situ compression tests on electron transparent W thin foils with and without He irradiation. To best witness the contrast, dislocation behaviors are compared for the W-0 and W-20 samples. Figure 2a shows a series of images extracted from the compressive video of W-0 (Movie S1). Initially the W-0 crystal contains a high density of defects, likely from cutting the pillar. Upon loading, these defects are seen to move and grow as dislocation loops and eventually leave the crystal. Their motion causes the W-0 sample to yield. As the strain increases to 2.5%, more of these initial dislocations move, leading to strain bursts. They eventually move out of the crystal, and the defect density experiences a marked decrease. By the time the strain increases to 5%, many of the defects have cleared the sample, and only some long straight screw-character dislocations remain, as seen in the in situ video (Movie S1). Long straight screw dislocations are common in deformed BCC metals, due to their substantially low mobility compared to nonscrew dislocations at ambient temperature.[25] As no new defects are produced during deformation, the net density of defects continually decreases with strain until only a few dislocation segments remain by strains of 10 and 15%. As a result, the material does not strain harden. At the end, we see that most of the deformation is accommodated by dislocation glide concentrated in a slip step at the right edge of the crystal. Such localized deformation explains the jerky flow and unstable plasticity signified in the corresponding stress−strain curve.

For comparison, Figure 2b presents images taken from the compression test video of the most highly irradiated sample, W-20 (Movie S2). It contains numerous dislocation loops and segments, and He bubbles, 1−2 nm in diameter, which are expected consequences of irradiation. When strain is applied, these dislocations glide, but not as easily as seen earlier in pure W. They move in a stick−slip manner and jump in small steps from one position to another. For example, we see that the glide behavior for a small curved dislocation involves advances via a series of bowing out events (Movie S2), indicating that motion is difficult. While they eventually leave the crystal, new dislocations nucleate from the He bubbles or other existing defects.[14−16] As a result, the dislocation density does not decrease with strain. Even at strains of 10 and 15%, the

https://doi.org/10.1021/acs.nanolett.1c01637
Nano Lett. 2021, 21, 5798−5804

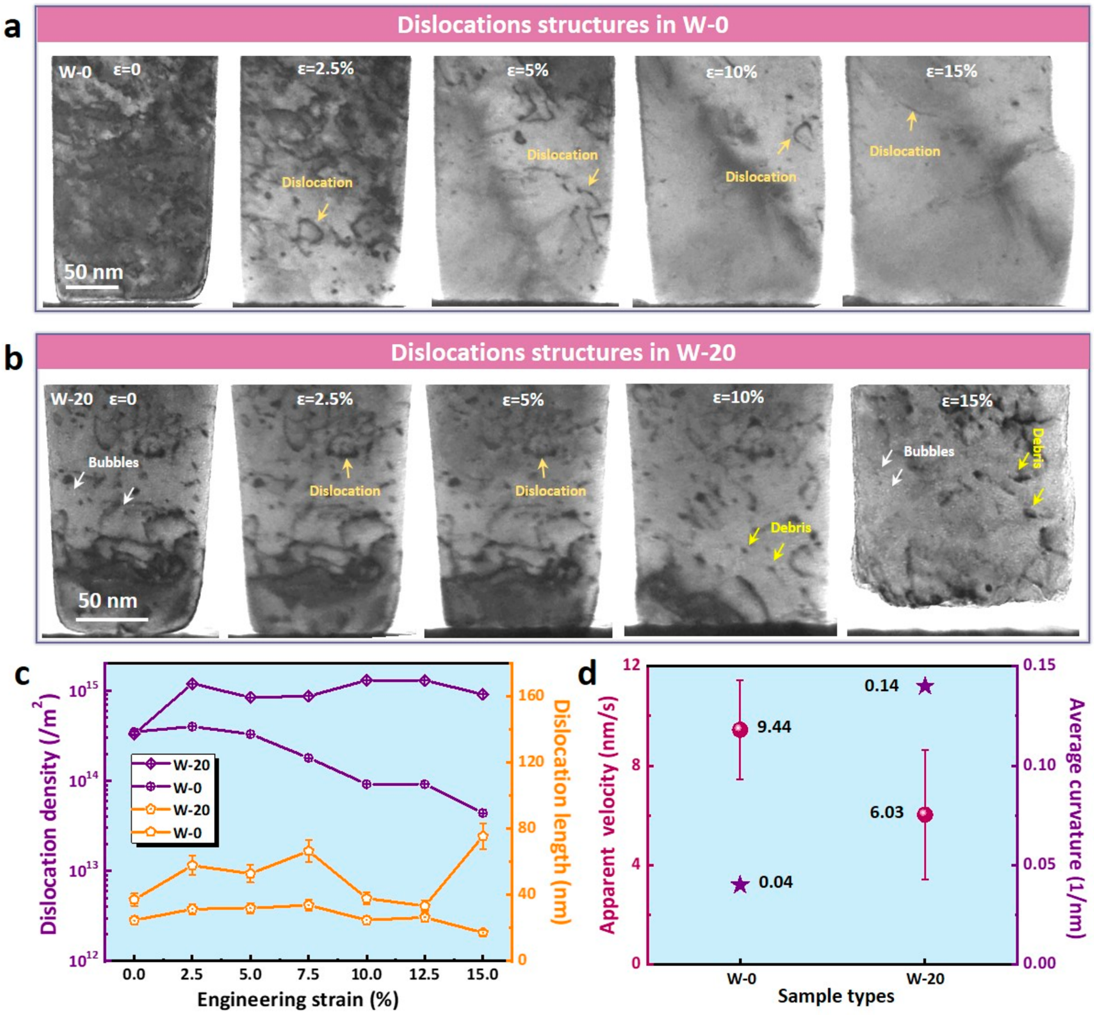

Figure 2. Dynamics of dislocations under straining in W. (a) Dislocations moving fast and disappearing at the surface in pure W under straining. (b) Dislocations bowing out slowly and being trapped by radiation defects. (c) Evolution of dislocation density and length with increasing strain. (d) Comparison of dislocation slip velocity and curvatures in pure W and W-20.

dislocation debris is everywhere in such a 30 nm thick foil, as indicated by the black dots in the images (Figure 2b). This explains the straining hardening and stable plasticity seen in the W-20 crystal. Even at the end of compression, many residual dislocations still remain in the W-20 thin foil. The size of He bubbles is increased after compression due to dislocation−bubble interactions,[14−16] as shown in Movie S2.

Glide difficulty for a collection of dislocations can be assessed on the basis of the rate dislocations accumulated in the sample as strain is increased and on their average velocity. In Figure 2c, the variation in dislocation density and dislocation length with strain are compared for material with different He concentrations. In the W-20 crystal, the dislocation density increases slightly during straining and until it saturates at $1 \times 10^{15}/m^2$ at a final strain of 15%. However, in the W-0 crystal, the dislocation density continuously decreases to a level of $10^{13}/m^2$. The average dislocation length remains constant in W-20, while they are much longer in the final stages and fluctuate with straining in W-0. The shorter dislocations in the W-20 move slower, on average two-thirds slower, than the longer dislocations in W-0 (Figure 2d). The dislocation velocity measured in W-0 is a conservative estimate since dislocations can move much faster than can be captured by the time resolution of the video camera.

Wavy dislocation morphologies serve as another sign of glide difficulty. Figure 3 shows examples of the evolution of the morphology of many individual dislocations in the W-0 and W-20 samples under high-resolution TEM observation. Note that even under high resolution, the region shown in the W-20 crystal is nearly free of visible irradiation defects just like the W-0 crystal. In W-0, the two long dislocations seen are initially straight. Under increasing strain, we witness only a slight bowing out in the middle part or near the head of the dislocation, as labeled by yellow lines in Figure 3a. In W-20, the one dislocation shown in Figure 3b is initially short, approximately 7 nm in length. As strain is applied and increased, the movement of the dislocation is distinct from that of the dislocations in W-0. The dislocation starts to bow out and form into a half-loop; then the diameter of the loop increases thereafter. With further loading, some portions of the loop move forward such that the loop takes on an elliptical shape, before finally leaving the crystal at the sample surface. The curvature in the dislocation line is proportional to the resistance to dislocation glide. The average dislocation curvature in W-20 is measured to be 3.5 times of that in W-

https://doi.org/10.1021/acs.nanolett.1c01637
Nano Lett. 2021, 21, 5798−5804

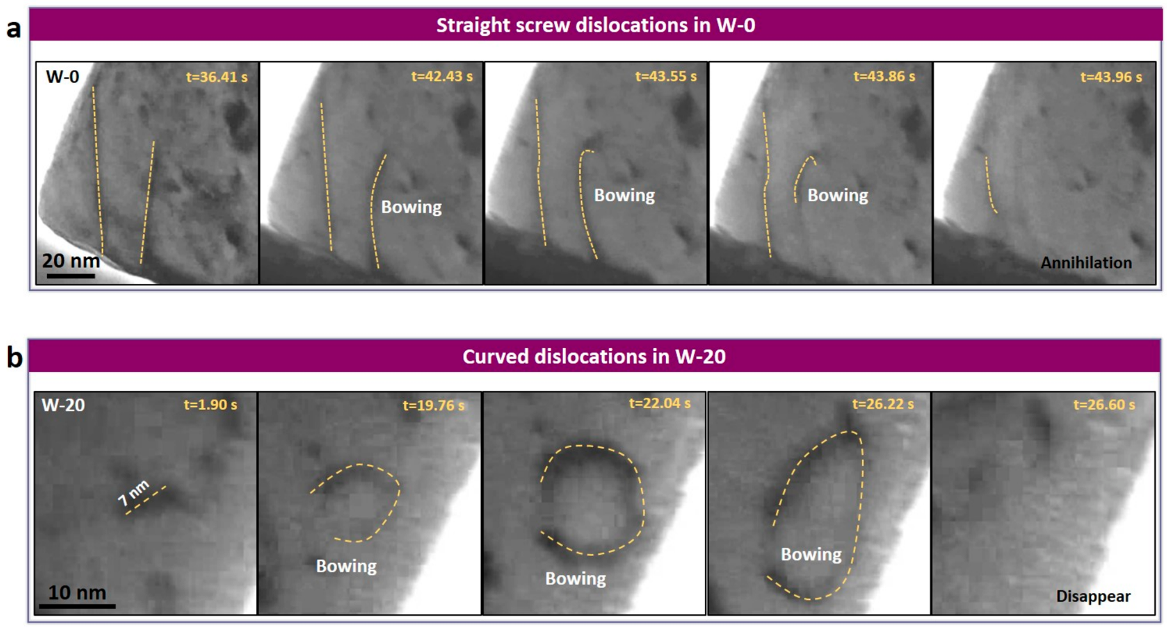

Figure 3. Bowing out of dislocations under straining. (a) Straight screw dislocations produced in pure W under straining. (b) Dislocations obstructed by hidden radiation defects, forming a bow-out configuration in W-20. This behavior indicates that the mobility of edge and screw dislocations are comparable in this case.

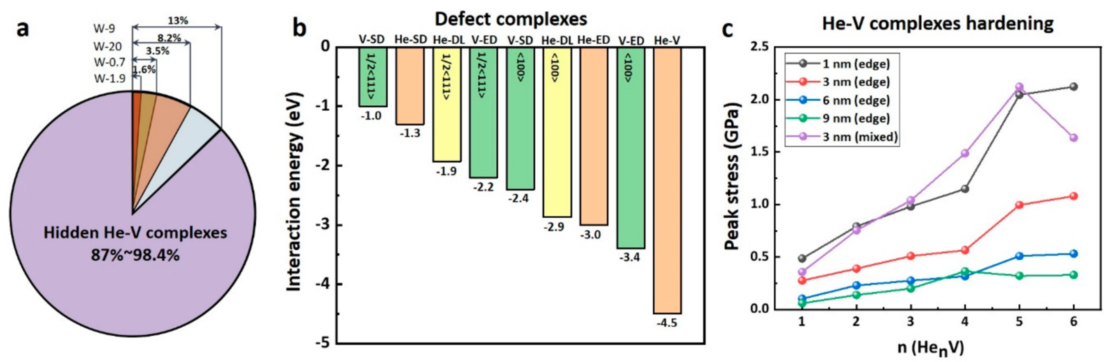

Figure 4. Hidden He−V complexes and their interaction with dislocations. (a) Percentage of helium bubbles and hidden He−V complexes in the matrix. (b) Interaction energy of defect complexes.[35−37] (c) Hardening by dislocation−He−V complex interactions in irradiated W.

0, which is consistent with the nearly 3 times increase in the yield strength in W-20 over W-0, as seen in Figure 1. In theory, the maximum stress required to move this dislocation through this sequence is that associated with overcoming line tension to form a half-loop between the l = 7 nm pinning points. Using values for W, this stress is estimated by $\tau = \frac{\alpha G b}{l}$ (where G = 161 GPa is the shear modulus, b is the value of the Burgers vector of dislocation, l is the spacing of the initially straight dislocation segment between pinning points, and α = 0.2 for helium bubbles with sizes less than 2 nm[26−28]), to be no less than 1.26 GPa. This value is unusually high, signifying that it was difficult to move this dislocation in the irradiated W-20 sample.

Material hardening by irradiation is estimated on the basis of the size and distribution of irradiation defects, such as bubbles, observable by state-of-the-art microscopy. Three analytical models have been applied to forecast material hardening: Bacon−Orowan, Friedel equation, and DBH models,[26−28] (see the SI for detailed formulations). These models predict $\Delta\tau$, the increment in critical resolved shear stress ($\Delta\tau$) experienced by a dislocation gliding on a plane containing an array of bubbles, with a given spacing, diameter, and pressure. They differ, however, in the penetrability of bubble, from sliceable (Bacon−Orowan) to impenetrable (DBH). On the basis of extensive TEM microstructure measurements of bubble size and spacing, their internal pressure and density were calculated (see Table S1). The corresponding $\Delta\tau$ estimates from the Bacon−Orowan, Friedel equation, and DBH models[26−28] are shown in Figure 1b and compared with $\Delta\tau$ extracted from the deformation behavior in Figures 1−3. The $\Delta\tau$ in irradiated W pillars ranges from 0.75 to 1.6 GPa, which is outstandingly greater (by 60%) than all model predictions. These same hardening models, despite their different assumptions, typically predict $\Delta\tau$ in FCC, HCP, and nanolaminated metals,[14−18,26−28] well within 10%. The large 60% gap between theory and experiments strongly indicates that hardening in irradiated W cannot be explained simply by the formation of He bubbles.

To identify the missing component contributing to irradiation hardening, we first compare the amount of He in TEM-visible bubbles and the total implanted He. The

https://doi.org/10.1021/acs.nanolett.1c01637
Nano Lett. 2021, 21, 5798−5804

implanted He in a specific pillar can be estimated via $N_{implanted} = X_{He}F$, where X_{He} is the atomic percentage of He ion at fixed depth, obtained from the stopping and range of ions in materials (SRIM) simulation (see Figure S1) and F is the fluence of ion implantation. X_{He} is averaged according to the size of the pillar and the number of He in bubbles. $N_{bubbles}$ is estimated according to the size and internal pressure of the bubbles.[26−31] We used three different methods to calculate the average He per bubble (see the SI for details). Figure 4a shows that all methods indicate that the percentage of He ions in the He bubbles corresponds only to a small fraction of the total, ranging, on average, from just 1.6% for W-1.9 to at most 13% for W-9. Remarkably, most of the implanted He atoms still reside in the lattice but outside of the He bubbles. For comparison, we performed similar calculations on He-implanted metals with distinct crystal structure, FCC and HCP.[14−18] In these metals, nearly 100% of the He atoms are found in the TEM-visible bubbles. However, clearly in W, the majority of the irradiation defects are still dispersed in the lattice at an atomic scale, undetectable by high-resolution TEM.

The unexpected defect distribution raises two questions. First, why does the large fraction of irradiation defects in W, as well as BCC metals in general, not diffuse and coalesce even after high-temperature irradiation? Second, is the well-known UIH in BCC metals related to large amounts of the TEM-invisible defects? To address these questions, it is essential to first consider the mobility of irradiation point defects in W and the binding energy of dislocations with these point defects. According to ab initio calculation, self-interstitials are highly mobile, while vacancies in W have a migration energy of 1.7 eV, which is at least two to three times that for FCC and HCP metals.[32−34] In general, most vacancy (V) migration energies in refractory metals are larger than 1 eV, explaining the difficulty in the migration and clustering of vacancies that is characteristic of BCC metals, especially Cr, Mo, and W.[28] Therefore, it is plausible that irradiation-induced vacancies would be largely "frozen" in the lattice in BCC metals after irradiation unlike in FCC or HCP metals.

Figure 4b summarizes the interaction energies of typical defects in irradiated W, such as He−V, He-dislocation, and V-dislocation.[35−37] There is a strong interaction between He and V, such as an interaction energy of −4.5 eV, which is the lowest among all kinds of defects in Figure 4b. As a result, He ions are likely to bind to a vacancy in W. The large quantity of hidden He atoms are, therefore, an indication of hidden vacancies in the W lattice. Together, they would form numerous stable He−V complexes, the sizes of each being sufficiently small to evade detection by microscopy.

We also note from Figure 4b the strong binding between dislocations and He/V, indicating a strong pinning effect on dislocation by those defect complexes. In particular, edge dislocations are much more strongly attracted to the He/V than screw dislocations, which would suggest that the reduction in dislocation mobility, due to the He/V alone, would be greater for the edge than the screw dislocation. In previous work, the interaction of He−V clusters with edge dislocations was found strongly attractive in α-Fe,[38,39] and this effect is similar to the obstruction of V−O complexes on screw dislocation in Nb.[25] Consequently, the presence of complexes could lower the usual significant gap in mobilities between screw and edge dislocations characteristic of pure BCC metals. This implication is consistent with the in situ observations made in Figures 2 and 3. The expanding dislocations in irradiated W under deformation are nearly circular, indicating that the edge and screw dislocation mobilities are similar in value. Such is not the case in pure W (Figure 3a), where a screw dislocation moves much slower than an edge, causing dislocation loops to expand anisotropically leaving relatively long, straight-line screw dislocations.[40]

To understand the effect complexes have on dislocation motion, we carry out MD simulations of gliding dislocations interacting with a He−V complex. Due to the anticipated effect of character, simulations are repeated for an edge character dislocation and a mixed character dislocation with nearly screw orientation. Since the number of He atoms that can bind stably to a vacancy in any given complex can vary from 1 to 6, in simulation, we consider the full 1-to-6 range of He:V ratios. Taking into account the high fraction of undetected He atoms (over 80%), these ratios translate to a broad span of L_{He-V}, He:V complex spacings, 1−9 nm. In simulation, the dislocation becomes pinned upon impinging on the complex, and provided that an applied critical stress is exceeded, it depins from the complex, leaving the complex still intact as a cluster. Figure 4c plots this critical stress versus He:V complex ratio when assuming a fixed L_{He-V}. In all cases, the dislocations require higher stresses in order to bypass the complex than without, although the additional force required depends sensitively on the size of the complex (number of He atoms) and the spacing between two neighboring complexes. Both mixed and edge dislocations need substantially higher stresses, ranging from 0.5 to 1 GPa, to depin from the complex with smaller L_{He-V}. Notably the critical stress for the mixed dislocation, being nearly screw-oriented with a 19.5° character angle, can be substantial, ranging from 0.5 to 2 GPa for the range of He:V studied. The strengthening prevails provided that the dislocation does not cross slip over the complex, which occurs when He:V = 6. The calculations also confirm that the screw to edge stress ratio reduces to 2−3, which is a substantial reduction from 10 to 20, the ratios without complexes.[41]

With the support from MD simulation results and in situ nanomechanical tests (Figures 2 and 3), we propose that, in addition to those TEM-visible He bubbles, large quantities of hidden He, vacancies, or He−V complexes obstruct the motion of dislocations in irradiated W (because of $L_{He-V} \ll L_{bubble}$), especially for nonscrew dislocations, as indicated in Figure 4c. According to the irradiation hardening increment in Figure 1b and the Friedel hardening model,[27] the average spacing of He−V complexes is about 3−6 nm for W-9 and W-20 pillars. In this case, the size of He−V complexes is only several angstroms, which is invisible in a defected sample under normal TEM observations. For these sizes, the MD simulations indicate that complex spacings in this range of L_{He-V} can explain the remarkable boost in shear strength of 1 GPa.

In summary, ultrahigh-irradiation hardening in W originates from the strong interaction of dislocations with TEM-visible He bubbles and those atomic-scale hidden defects, especially vacancies and He-V complexes. In situ nanomechanical tests and MD calculations identify that these complexes serve as strong pinning points, especially for edge dislocations, raising the critical stress to depin the dislocation by more than 1 GPa. This mechanism is ubiquitous in BCC metals at low- to medium-temperature range because of their exceptionally high vacancy migration energy.

https://doi.org/10.1021/acs.nanolett.1c01637
Nano Lett. 2021, 21, 5798−5804

■ ASSOCIATED CONTENT

Supporting Information

The Supporting Information is available free of charge at https://pubs.acs.org/doi/10.1021/acs.nanolett.1c01637.

Experimental methods for helium implantation and nanomechanical testing and calculation methods for helium bubble strengthening and helium partitioning in bubble and matrix (PDF)

Movie S1 showing compression of W-0 crystal and impact on defects (MP4)

Movie S2 showing compression of W-20 crystal and impact on defects (MP4)

■ AUTHOR INFORMATION

Corresponding Author

Wei-Zhong Han − *Center for Advancing Materials Performance from the Nanoscale, State Key Laboratory for Mechanical Behavior of Materials, Xi'an Jiaotong University, Xi'an 710049, China;* orcid.org/0000-0001-7982-4042; Email: wzhanxjtu@mail.xjtu.edu.cn

Authors

Ruo-Yao Zheng − *Center for Advancing Materials Performance from the Nanoscale, State Key Laboratory for Mechanical Behavior of Materials, Xi'an Jiaotong University, Xi'an 710049, China*

Wu-Rong Jian − *Department of Mechanical Engineering, University of California, Santa Barbara, California 93106-5070, United States*

Irene J. Beyerlein − *Department of Mechanical Engineering, University of California, Santa Barbara, California 93106-5070, United States; Materials Department, University of California, Santa Barbara, California 93106-5070, United States*

Complete contact information is available at: https://pubs.acs.org/10.1021/acs.nanolett.1c01637

Author Contributions

W.-Z.H. conceived the project. R.-Y.Z. performed the experiments under the guidance of W.-Z.H. W.-R.J. and I.J.B. performed the molecular dynamic simulations. R.-Y.Z., I.J.B., and W.-Z.H wrote the manuscript. All of the authors discussed and analyzed the data and have given approval to the final version of the manuscript.

Notes

The authors declare no competing financial interest.

■ ACKNOWLEDGMENTS

We thank Prof. Ju Li (MIT) and Prof. Fei Gao (University of Michigan) for fruitful discussion. This research was supported by the National Natural Science Foundation of China (Grant Nos. 51971170, 51922082, and 51942104), the National Key Research and Development Program of China (Grant No. 2017YFB0702301), the 111 Project of China (Grant No. BP2018008), and the Innovation Project of Shaanxi Province (Grant No. 2017KTPT-12).

■ REFERENCES

(1) Gilbert, M. R.; et al. Neutron-induced dpa, transmutations, gas production, and helium embrittlement of fusion materials. *J. Nucl. Mater.* **2013**, *442*, S755−S760.

(2) Zinkle, S. J.; Snead, L. L. Designing radiation resistance in materials for fusion energy. *Annu. Rev. Mater. Res.* **2014**, *44*, 241−267.

(3) Knaster, J.; Moeslang, A.; Muroga, T. Materials research for fusion. *Nat. Phys.* **2016**, *12*, 424−434.

(4) Tong, Z.; Dai, Y. Tensile properties of the ferritic martensitic steel F82H after irradiation in a spallation target. *J. Nucl. Mater.* **2009**, *385*, 258−261.

(5) Maloy, S. A.; James, M. R.; Sommer, W., Jr.; Willcutt, G. J., Jr.; Lopez, M.; Romero, T. J.; et al. The effect of 800 MeV proton irradiation on the mechanical properties of tungsten. *Mater. Trans.* **2002**, *43*, 633−637.

(6) Miyazawa, T.; et al. Neutron irradiation effects on the mechanical properties of powder metallurgical processed tungsten alloys. *J. Nucl. Mater.* **2020**, *529*, 151910.

(7) Schaeublin, R.; Gelles, D.; Victoria, M. Microstructure of irradiated ferritic/martensitic steels in relation to mechanical properties. *J. Nucl. Mater.* **2002**, *307−311*, 197−202.

(8) Tanigawa, H.; Klueh, R. L.; Hashimoto, N.; Sokolov, M. A. Hardening mechanisms of reduced activation ferritic/martensitic steels irradiated at 300 °C. *J. Nucl. Mater.* **2009**, *386−388*, 231−235.

(9) Argon, A. S.; Maloof, S. R. Plastic deformation of tungsten single crystals at low temperature. *Acta Metall.* **1966**, *14*, 1449−1462.

(10) Gludovatz, B.; Wurster, S.; Hoffmann, A.; Pippan, R. Fracture toughness of polycrystalline tungsten alloys. *Int. J. Refract. Hard Met.* **2010**, *28*, 674−678.

(11) Rowcliffe, A. F.; et al. Austenitic stainless steels and high strength copper alloys for fusion components. *J. Nucl. Mater.* **1998**, *258−263*, 183−192.

(12) Byun, T. S.; Farrell, K. Plastic instability in polycrystalline metals after low temperature irradiation. *Acta Mater.* **2004**, *52*, 1597−1608.

(13) Hu, X. X.; et al. Irradiation hardening of pure tungsten exposed to neutron irradiation. *J. Nucl. Mater.* **2016**, *480*, 235−243.

(14) Ding, M. S.; et al. Radiation-induced helium nanobubbles enhance ductility in submicron-sized single-crystalline copper. *Nano Lett.* **2016**, *16*, 4118−4124.

(15) Ding, M. S.; et al. Nanobubble fragmentation and bubble-free-channel shear localization in helium irradiated submicron-sized copper. *Phys. Rev. Lett.* **2016**, *117*, 215501.

(16) Li, S. H.; Zhang, J.; Han, W. Z. Helium bubbles enhance strength and ductility in small-volume Al-4Cu alloys. *Scr. Mater.* **2019**, *165*, 112−116.

(17) Kiener, D.; Hosemann, P.; Maloy, S. A.; Minor, A. M. In situ nanocompression testing of irradiated copper. *Nat. Mater.* **2011**, *10*, 608−613.

(18) Liu, S. M.; Li, S. H.; Han, W. Z. Effect of ordered helium bubbles on deformation and fracture behavior of α-Zr. *J. Mater. Sci. Technol.* **2019**, *35*, 1466−1472.

(19) Philipps, V. Tungsten as material for plasma-facing components in fusion devices. *J. Nucl. Mater.* **2011**, *415*, S2−S9.

(20) Hou, J.; Kong, X. S.; Wu, X. B.; Song, J.; Liu, C. S. Predictive model of hydrogen trapping and bubbling in nanovoids in bcc metals. *Nat. Mater.* **2019**, *18*, 833−839.

(21) Iwakiri, H.; Yasunaga, K.; Morishita, K.; Yoshida, N. Microstructure evolution in tungsten during low-energy helium ion irradiation. *J. Nucl. Mater.* **2000**, *283−287*, 1134−1138.

(22) Armstrong, D. E. J.; Edmondson, P. D.; Roberts, S. G. Effects of sequential tungsten and helium ion implantation on nano-indentation hardness of tungsten. *Appl. Phys. Lett.* **2013**, *102*, 251901.

(23) Ou, X.; Anwand, W.; Kögler, R.; Zhou, H. B.; Richter, A. The role of helium implantation induced vacancy defect on hardening of tungsten. *J. Appl. Phys.* **2014**, *115*, 123521.

(24) Das, S.; et al. The effect of helium implantation on the deformation behaviour of tungsten: X-ray micro-diffraction and nanoindentation. *Scr. Mater.* **2018**, *146*, 335−339.

(25) Yang, P. J.; et al. Mechanism of hardening and damage initiation in oxygen embrittlement of body-centred-cubic niobium. *Acta Mater.* **2019**, *168*, 331−342.

(26) Li, N.; Nastasi, M.; Misra, A. Defect structures and hardening mechanisms in high dose helium ion implanted Cu and Cu/Nb multilayer thin films. *Int. J. Plast.* **2012**, *32–33*, 1–16.
(27) Wei, Q. M.; Li, N.; Mara, N.; Nastasi, M.; Misra, A. Suppression of irradiation hardening in nanoscale V/Ag multilayers. *Acta Mater.* **2011**, *59*, 6331–6340.
(28) Hu, X. X.; Xu, D. H.; Byun, T. S.; Wirth, B. D. Modeling of irradiation hardening of iron after low-dose and low-temperature neutron irradiation. *Modell. Simul. Mater. Sci. Eng.* **2014**, *22*, 065002.
(29) Polian, A.; Grimsditch, M. Elastic Properties and Density of Helium up to 20 GPa. *Europhys. Lett.* **1986**, *2*, 849–855.
(30) Landau, P.; Guo, Q.; Hosemann, P.; Wang, Y. Q.; Greer, J. R. Deformation of as-fabricated and helium implanted 100 nm-diameter iron nano-pillars. *Mater. Sci. Eng., A* **2014**, *612*, 316–325.
(31) Villacampa, I.; Chen, J. C.; Spätig, P.; Seifert, H. P.; Duval, F. Helium bubble evolution and hardening in 316L by post-implantation annealing. *J. Nucl. Mater.* **2018**, *500*, 389–402.
(32) Balluffi, R. W. Vacancy defect mobilities and binding energies obtained from annealing studies. *J. Nucl. Mater.* **1978**, *69–70*, 240–263.
(33) Vérité, G.; Willaime, F.; Fu, C. C. Anisotropy of the vacancy migration in Ti, Zr and Hf hexagonal close-packed metals from first principles. *Solid State Phenom.* **2007**, *129*, 75–81.
(34) Schultz, H. Vacancy migration in BCC transition metals. *Scr. Metall.* **1974**, *8*, 721–726.
(35) Bakaev, A.; Terentyev, D.; Grigorev, P.; Posselt, M.; Zhurkin, E. E. Ab initio study of interaction of helium with edge and screw dislocations in tungsten. *Nucl. Instrum. Methods Phys. Res., Sect. B* **2017**, *393*, 150–154.
(36) Grigorev, P.; et al. Interaction of hydrogen and helium with nanometric dislocation loops in tungsten assessed by atomistic calculations. *Nucl. Instrum. Methods Phys. Res., Sect. B* **2017**, *393*, 164–168.
(37) Chen, Z. M.; Mrovec, M.; Gumbsch, P. Dislocation–vacancy interactions in tungsten. *Modell. Simul. Mater. Sci. Eng.* **2011**, *19*, 074002.
(38) Yang, L.; et al. Interaction of helium–vacancy clusters with edge dislocations in a-Fe. Nucl. *Nucl. Instrum. Methods Phys. Res., Sect. B* **2007**, *265*, 541–546.
(39) Yang, L.; et al. Dynamic interactions of helium-vacancy clusters with edge dislocations in a-Fe. *Phys. B* **2010**, *405*, 1754–1758.
(40) Caillard, D. Geometry and kinetics of glide of screw dislocations in tungsten between 95K and 573K. *Acta Mater.* **2018**, *161*, 21–34.
(41) Wang, X.; et al. *Comput. Mater. Sci.* **2021**, *192*, 110364.

https://doi.org/10.1021/acs.nanolett.1c01637
Nano Lett. 2021, 21, 5798–5804